

# Which Forces Control Supracrystal Nucleation in Organic Media?

Nicolas Goubet, Johannes Richardi, Pierre-Antoine Albouy, and Marie-Paule Pileni\*

Here, two mechanisms of fcc Au supracrystal (assembly of Au nanocrystals) growth are proposed. The sizes of the Au nanocrystals and the solvent in which they are dispersed are major parameters that determine the final morphology of nanocrystal assemblies; films by layer-by-layer growth (heterogeneous growth), characterized by their plastic deformation, or well-defined shapes grown in solution (homogeneous growth). Experiments supported by simulations demonstrate that supracrystal nucleation is mainly driven by solvent-mediated interactions and not solely by the van der Waals attraction between nanocrystal cores, as widely assumed in the literature.

## 1. Introduction

Nanomaterials are as old as the world. Thus, there are strong indications that nanoparticles such as fullerenes may exist in the interstellar medium.<sup>[1]</sup> In biology, nanomaterials are synthesized in a rather large number of animals and bacteria.<sup>[2]</sup> In art, nanoparticles have been used for more than 2000 years as dyes in ceramics and painting because their colors differ with their sizes and shapes.<sup>[3]</sup> In metallurgy, cementite nanoparticles are used to improve the mechanical properties of the Damascus steel in order to make high quality blades.<sup>[4]</sup>

Spherical objects like balls or nanomaterials having a uniform diameter self-organize in compact hexagonal networks (2D) or stack in 3D layers. The first discovery of a large scale assembly, at the mesoscopic scale, of nanocrystals into periodic arrangements is the well-known opal made with submicron silica particles with a marked change in its optical properties with the particle's ordering. In fact for a disordered assembly of silica particles a colorless opal is produced whereas, when the particles are ordered; specific reflectivity related to the size of the self-assembled particles is observed.<sup>[5]</sup>

Nanocrystals can be assembled in structures of various dimensionalities inducing different collective properties. The

linear 1D chains of nanocrystals behave as homogeneous nanowires as in the magnetosome extracted from magnetostatic bacteria.<sup>[6]</sup> Collective optical and magnetic properties due to dipolar interactions are observed when the nanocrystals are organized in 2D superlattices.<sup>[7]</sup> When the nanocrystals are self-ordered in 3D fcc arrangements called supracrystals, new collective mechanical, vibrational, and magnetic properties are observed.<sup>[8,9]</sup> This clearly shows that periodic arrangements, control of the interparticle distances and surface chemistry are key

steps for obtaining solid-state materials with tunable chemical, electronic, and magnetic properties. These novel artificial tailored materials have huge potential both for fundamental research<sup>[7–14]</sup> and applications ranging from magnetic storage to electronic and optical devices.<sup>[15]</sup> Good definition of nanocrystals in size and shape is a prerequisite to their arrangement on a Bravais lattice (called “supracrystal”), but which crystalline structure is finally reached may be influenced by such parameters as the temperature, solvents, coating agents, etc.<sup>[7,8,16–24]</sup>

The close stacking of nanocrystals makes possible formation of face centered cubic (fcc) and hexagonal compact packing (hcp) crystals.<sup>[19,25,26]</sup> In these, as well as body centered cubic (bcc) crystals, the nanocrystals are regularly arranged, while disordered particles make up solids called “amorphous”. Note that in many crystalline phase diagrams of bulk metals, depending on the temperature and pressure, two phases are obtained.<sup>[27,28]</sup> The nanocrystal crystalline structures can be tuned either with their sizes<sup>[29,30]</sup> or the pressure.<sup>[31]</sup> Very recently it has been found that Ag nanocrystals are able to self-assemble in supracrystals of different structures (such as fcc and hcp or hcp and bcc supra crystals) at a fixed pressure using different temperatures.<sup>[32]</sup> While various types of mesoscopic materials have been produced, there is however no general understanding as to which parameters control the supracrystal growth. Preliminary study shows that one of the major parameters is the solvent used to disperse the nanocrystals.<sup>[33]</sup>

Here we propose two supracrystal growth mechanisms. The nanocrystal size, coating agent, and its solvation are key parameters in the final morphology of periodic arrangements with either a layer-by-layer growth or a process of nucleation and growth in solution. Experiments sustained by simulations presently demonstrate that supracrystal nucleation is mainly driven by solvent-mediated interactions and not only by the van der Waals attraction between nanocrystal cores as widely assumed in the literature.<sup>[20,21]</sup>

N. Goubet, J. Richardi, Prof. M.-P. Pileni  
Université Pierre et Marie Curie  
and Centre National de la Recherche Scientifique  
UMR 7070, LM2N  
4 Place Jussieu, 75005 Paris, France  
Tel: (33) 1 44 27 25 78  
E-mail: marie-paule.pileni@upmc.fr  
P.-A. Albouy  
Laboratoire de Physique des Solides  
Université Paris-Sud, 91405 Orsay, France  
E-mail: albouy@lps.u-psud.fr

DOI: 10.1002/adfm.201100382

## 2. Theory

To understand the evolution of order and morphology of superlattices with the nanocrystal diameter and solvent, the assembly of Au nanocrystals is simulated at a particle level. We will first introduce the model of interaction between the nanocrystals and, then, explain both theoretical methods employed, i.e., Brownian dynamics and Monte Carlo simulations.

### 2.1. The Interaction Model for Coated Au Nanocrystals

The interaction potential between the nanocrystals is defined as a sum of three terms:

$$u_{\text{tot}}(r) = u_{\text{vdW}}(r) + u_{\text{mix}}(r) + u_{\text{elastic}}(r) \quad (1)$$

where  $r$ ,  $u_{\text{vdW}}(r)$ ,  $u_{\text{mix}}(r)$ , and  $u_{\text{elastic}}(r)$  are the center-center distance between the nanocrystals, the van der Waals attraction between the metallic cores of the particles, the free energy of mixing of the thiol ligands, and the elastic compression of the ligands, respectively.

The three interaction terms are discussed in the following:

- (i) The van der Waals attraction between the nanocrystal cores,  $u_{\text{vdW}}(r)$ , is calculated from the usual equation<sup>[34]</sup>

$$u_{\text{vdW}}(r) = -\frac{A}{12} \left[ \frac{d^2}{r^2 - d^2} + \frac{d^2}{r^2} + 2 \ln \left( 1 - \frac{d^2}{r^2} \right) \right] \quad (2)$$

where  $A$  is the effective Hamaker constant of gold which is reduced with respect to its value in vacuum due to the presence of the solvent medium. In previous studies,<sup>[35,36]</sup> a value of  $31.2 \times 10^{-20}$  J was used for the Hamaker constant. To investigate the influence of this value on the theoretical results, we propose to calculate a second value for the Hamaker constant from that measured for massive Au in vacuum. The effective Hamaker constant markedly reduced due to the presence of the solvent medium is calculated from the usual formula

$$A' = \left( \sqrt{A_{\text{gold}}} - \sqrt{A_{\text{solvent}}} \right)^2 \quad (3)$$

where  $A_{\text{gold}}$  and  $A_{\text{solvent}}$  are the Hamaker constants of Au and the solvent in air. The values for  $A_{\text{gold}}$  and  $A_{\text{solvent}}$  are taken from the literature<sup>[37,38]</sup> (in  $10^{-20}$  J; gold: 45.3; hexane: 4; toluene: 5.4; octane: 5.0; for cumene, the value of toluene is used). The Hamaker constants ( $A = 22.4 \times 10^{-20}$  J and  $19.4 \times 10^{-20}$  J for hexane and toluene, respectively) are significantly smaller than the first one used in the previous studies.

- (ii) The free energy of mixing of the thiol ligands,  $u_{\text{mix}}(r)$ : When two nanocrystals with their ligand layers approach, three different regimes must be distinguished. The first regime is defined by nanocrystal separations  $r > d + 2L$ , where  $L$  is the contour length of the ligands recorded previously<sup>[39]</sup> (for dodecanethiol: 1.774 nm). The free energy of mixing of the ligands can be neglected, since the ligand layers do not overlap. In the second regime ( $d + L < r < d + 2L$ ) the free energy of mixing is calculated from:

$$u_{\text{mix},1}(r) = \frac{\pi d}{2V_s} \phi_{\text{av}}^2 \left( \frac{1}{2} - \chi \right) [r - (d + 2L)]^2 \quad (4)$$

while in the third regime ( $d < r < d + L$ ) the free energy of mixing is given by:

$$u_{\text{mix},2}(r) = \frac{\pi d}{V_s} \phi_{\text{av}}^2 \left( \frac{1}{2} - \chi \right) \times L^2 \left[ 3 \ln \left( \frac{L}{r-d} \right) + 2 \left( \frac{r-d}{L} \right) - \frac{3}{2} \right] \quad (5)$$

Equation 4 and 5 were developed in the literature using the Flory theory of mixing.<sup>[40,41]</sup> In the following the parameters in both equations will be detailed. The volume  $V_s$  of the solvent molecule is calculated from the molecular weight and the density of the solvent (for toluene and hexane:  $1.78 \times 10^{-28}$  m<sup>3</sup> and  $2.182 \times 10^{-28}$  m<sup>3</sup>). The average volume fraction of the ligand segments in the thiol shell varies with the nanocrystal diameter. It is given by the following equations:

$$\Phi_{\text{av}} = N_{\text{ligand}} V_{\text{ligand}} / V_{\text{shell}} \quad (6)$$

$$N_{\text{ligand}} = A_{\text{core}} / A_{\text{ligand}} \quad (7)$$

where  $N_{\text{ligand}}$  is the number of ligands per nanocrystal. The molecular volume  $V_{\text{ligand}}$  of dodecanethiol is determined from its molecular weight and density. To calculate the volume  $V_{\text{shell}}$  of the ligand shell, it is assumed that the shell extends from  $r = d/2$  to  $r = d/2 + L$ .  $A_{\text{core}}$  is the total surface area of the nanocrystal core obtained from its diameter  $d$ . The average core surface area  $A_{\text{ligand}}$  covered by one thiol group is taken from the literature.<sup>[42]</sup> ( $A_{\text{ligand}} = 21.5 \text{ \AA}^2$ ). The Flory parameter  $\chi$  is given by the equation  $\chi = V_s / RT (\delta_s - \delta_m)^2 + \beta_1$ , where  $\delta_s$  and  $\delta_m$  are the Hildebrand solubility parameters of the solvent and the ligand taken from the literature<sup>[43,44]</sup> (values in  $10^4 \text{ Pa}^{0.5}$ ; toluene: 1.82; hexane: 1.49; octane: 1.51; cumene: 1.75 and 1.81; dodecane: 1.62). The parameter  $\beta_1$  is fixed at its usual value of 0.34.<sup>[36]</sup> We assume that only the alkane chains take part in the attraction. Therefore, the solubility parameter of dodecane is used for the solubility parameter of the ligand.

- (iii) The elastic contribution due to the ligand compression,  $u_{\text{elastic}}(r)$ , is neglected for particle separations  $r > d + L$ . At closer contact ( $r < d + L$ ) the chain is compressed between both nanocrystal cores. The following equation is taken from the literature:

$$\frac{u_{\text{elastic}}(r)}{kT} = \pi v d \left[ (r-d) \left( \ln \frac{L}{r-d} - 1 \right) + L \right] \quad (8)$$

where  $v$  is the number of ligands per unit area of the nanocrystal calculated from the equation:  $v = 1/A_{\text{ligand}}$ .

Kahn et al.<sup>[36]</sup> have recently used a similar interaction model to study the self-assembly of Au nanoparticles with a diameter of 5 nm in toluene.

### 2.2. Simulation Method

To take the influence of the solvent on the particle dynamics into account, Brownian dynamics simulations were carried out. The motion of the particles is described by the Langevin equation

$$\frac{\partial \vec{p}_i}{\partial t} = -\zeta_i \vec{p}_i + \vec{F}_i + \vec{F}_{r,i} \quad (9)$$

where  $\vec{p}_i$ ,  $\zeta_i$ ,  $\vec{F}_i$  and  $\vec{F}_{r,i}$  are the linear momentum, the friction coefficient and the interparticle and random force acting on the particle  $i$ . The Langevin equations are integrated using an algorithm proposed by Allen.<sup>[45]</sup> The friction coefficient is calculated from the Stokes law using the viscosity of hexane and toluene ( $10^{-3} \text{ kg m}^{-1} \text{ s}^{-1}$  at  $20^\circ \text{C}$ ). The time step for the simulation is 20 ps.

To examine the accuracy of the BD results, Monte Carlo simulations are carried out. The MC simulations are performed in the canonical ensemble using the Metropolis algorithm.<sup>[46]</sup> It involves random displacements in all three directions in space with the step length uniformly sampled from  $-\delta r/2$ ,  $\delta r/2$ . The value of  $\delta r$  is chosen to obtain an acceptance rate of 40%. For the simulations, the number of particles is 10000.

The formation of clusters during the simulation is first studied by snapshots, which show the positions of the particles in the simulation box. The structures in the snapshots can be directly compared to SEM images obtained after evaporation of the nanoparticle solutions. In order to compare the simulations made at different conditions, the cluster formation is analyzed in detail. The clusters are defined using a geometric criterion: two particles belong to the same cluster, if their interparticle distance is smaller than  $1.1(d + \delta)$ . Note that an energy criterion yields similar results, because the strong interparticle attraction inducing nucleation has a very short range and is isotropic. During the simulation run, the equilibration is monitored by the evolution of the internal excess energy, the average cluster size and the number of free particles. Only when these properties are converged within 2%, are the final structures analyzed. The size, form and internal structure of every cluster are investigated.

### 3. Synthesis of Au Nanocrystals Differing by Their Sizes

Au nanocrystals are synthesized by revisiting the Stucky method.<sup>[47]</sup> two solutions are used (for simplicity called A and B). A consists of 0.25 mmol of Chlorotriphenylphosphine Au(I) dissolved in 25 mL of toluene to which 125  $\mu\text{L}$  of dodecanthiol is added. The composition of B varies (see below). A and B are placed in a silicon bath at  $100^\circ \text{C}$  and are stirred until the products are dissolved to produce clear solutions and then mixed. The colorless and clear mixture turns slowly to brown and reaches a dark red solution. The colloidal solution is dried in a nitrogen flow and then ethanol

is added ( $V_{\text{ethanol}} = V_{\text{colloidal}}/3$ ) to the dark powder. After stirring, the solution is centrifuged and a black precipitate appears. The supernatant is removed. The black precipitate is dried in a nitrogen flow in order to eliminate the remaining ethanol. The Au nanocrystals are dispersed in toluene. To remove impurities and the precipitate, the resulting solution was centrifuged at 5000 rpm for 5 min. One drop of the colloidal solution is deposited on an amorphous carbon-coated copper grid placed on an absorbent paper. The solution B0 is composed of 2.5 mmol of tert-butylamine borane complex in 15 mL of toluene. As shown in Figure 1A the nanocrystals have a characterized by 7.8 nm as

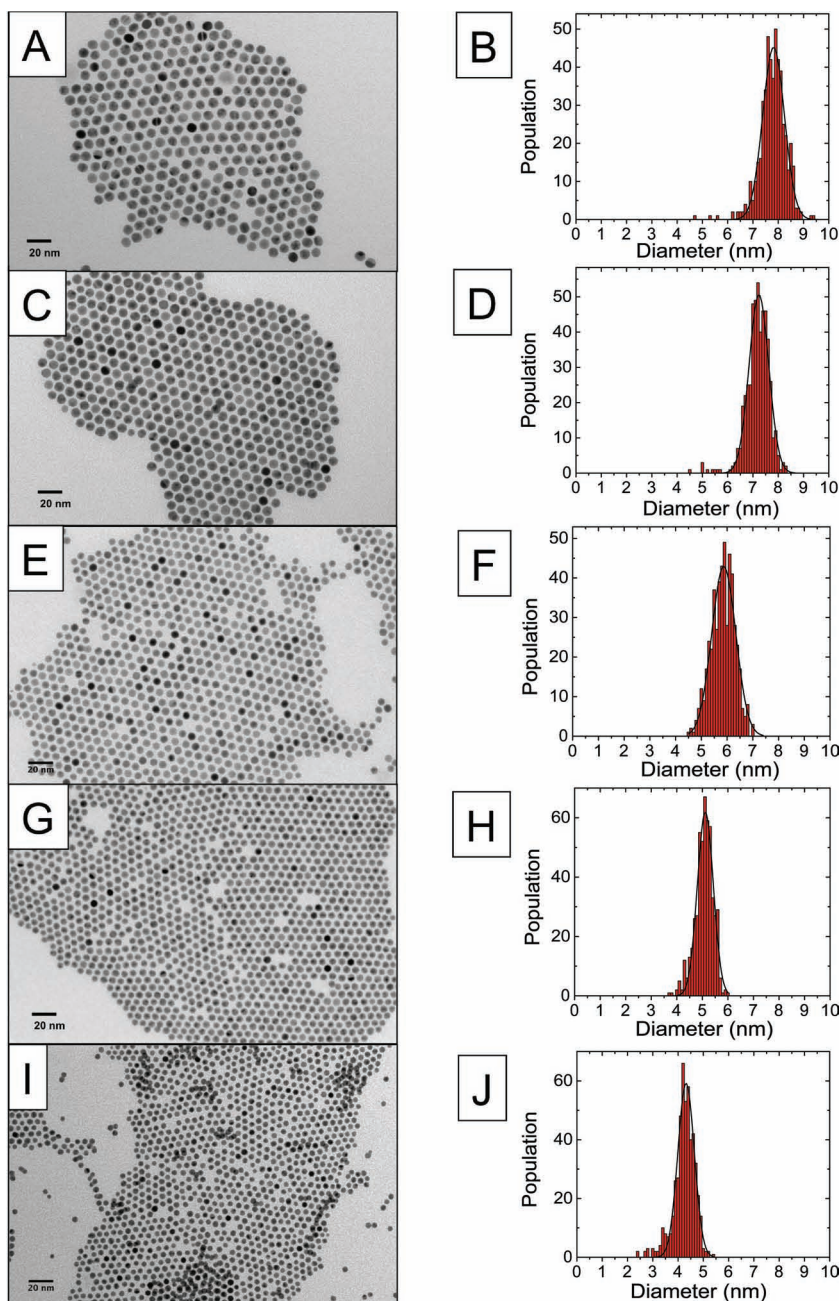


**Figure 1.** TEM picture of  $\text{Au}_8$ ,  $\text{Au}_7$ ,  $\text{Au}_6$ ,  $\text{Au}_5$  and  $\text{Au}_4$  (A, C, E, G, I respectively) and their corresponding size distribution (B, D, F, H, J).



average diameter with 6% as size dispersion (Figure 1B). Below, the nanocrystals corresponding to this synthesis are denoted Au<sub>8</sub>. Instead of adding 125  $\mu$ L of dodecanethiol to solution A as described above, either 250  $\mu$ L or 500  $\mu$ L is added. The procedure described above remains the same. At the end of the synthesis, the average diameters are reduced to 7.2 nm (Figure 1C) and 5.8 nm (Figure 1E) with 7% (Figure 1D) and 8% (Figure 1F) in diameter distribution, respectively. These samples will be denoted as Au<sub>7</sub> and Au<sub>6</sub>, respectively. Two B solutions are prepared. The first one B<sub>1</sub> is made of 5 mmol of tert-butylamine borane complex dissolved in 2 mL of toluene, while the second one B<sub>2</sub> is made of 2.5 mmol of ammonia-borane complex dissolved in a mixture of solvent ethanol/toluene (5 mL/10 mL). By mixing B<sub>1</sub> with A containing 500  $\mu$ L of dodecanethiol and using the same procedure described above, as shown in Figure 1G, the average nanocrystals diameter is 5.1 nm with 8% (Figure 1H) in size distribution (Au<sub>5</sub>). By replacing B<sub>1</sub> by B<sub>2</sub> the average nanocrystals diameter is reduced to 4.3 nm (Au<sub>4</sub>) (Figure 1I) with 9% in size distribution (Figure 1J).

#### 4. Results and Discussion

At the end of the evaporation of a colloidal solution with 100  $\mu$ L of Au nanocrystals ( $[Au_n] = 10^{-2}$  M) dispersed in toluene, the SEM images show a drastic change in the film morphology with the Au nanocrystal size (Figure 2). The SEM images obtained for Au<sub>8</sub> (Figure 2A and 2B), Au<sub>7</sub> (Figure 2C and 2D) and Au<sub>6</sub> (Figure 2E and 2F) nanocrystals show individual aggregates with well-defined shapes having an average size of 1  $\mu$ m to 10  $\mu$ m. Some of them are characterized by a very flat surface with well-defined edges whereas others show five-fold symmetry shape and still others without any characteristics symmetry shapes.<sup>[23,48]</sup> In contrast, uniform films covering most of the substrate with an average thickness of about 1  $\mu$ m are observed for Au<sub>4</sub> and Au<sub>5</sub> nanocrystals (Figure 2G, 2H and 2I, 2J). In order to better understand the structural differences between both organizations, small-angle X-ray diffraction (SAXD) is used. From the experimental reflections coordinates and the sample-detector distance obtained from SAXRD patterns (Figure 3A, 3C, 3E, 3G, 3I), the Bragg angle  $2\theta_B$  (Figure 3B, 3D, 3F, 3H, 3J) and thus the modulus of the diffracted vector  $q$  from the Bragg relation is obtained. Note that on figure 3H only one peak is observed, this is due to a short working distance. The distances in the reciprocal space are converted into  $d_{hkl}$ -spacings using the formula  $q = 2\pi/d_{hkl}$ . The expressions for the projected  $q_x$  and  $q_y$  values are:

$$q_{hkl}^x = \frac{2\pi}{D} \sqrt{\frac{h^2 + k^2 + l^2 - hk - kl - hl}{3}} \quad (10)$$

$$q_{hkl}^y = \frac{2\pi}{D} \frac{h + k + l}{\sqrt{6}} \quad (11)$$

for fcc packing, with  $D$  being the coated particle diameter. The interparticle spacing  $\delta$  is given by  $\delta = D - 2R$ , with  $R$  the average radius of the gold nanocrystals determined from TEM images. The width of the reflections is resolution-limited (Figure 3B, 3D, 3F, 3H, 3J) indicating average supracrystal dimensions

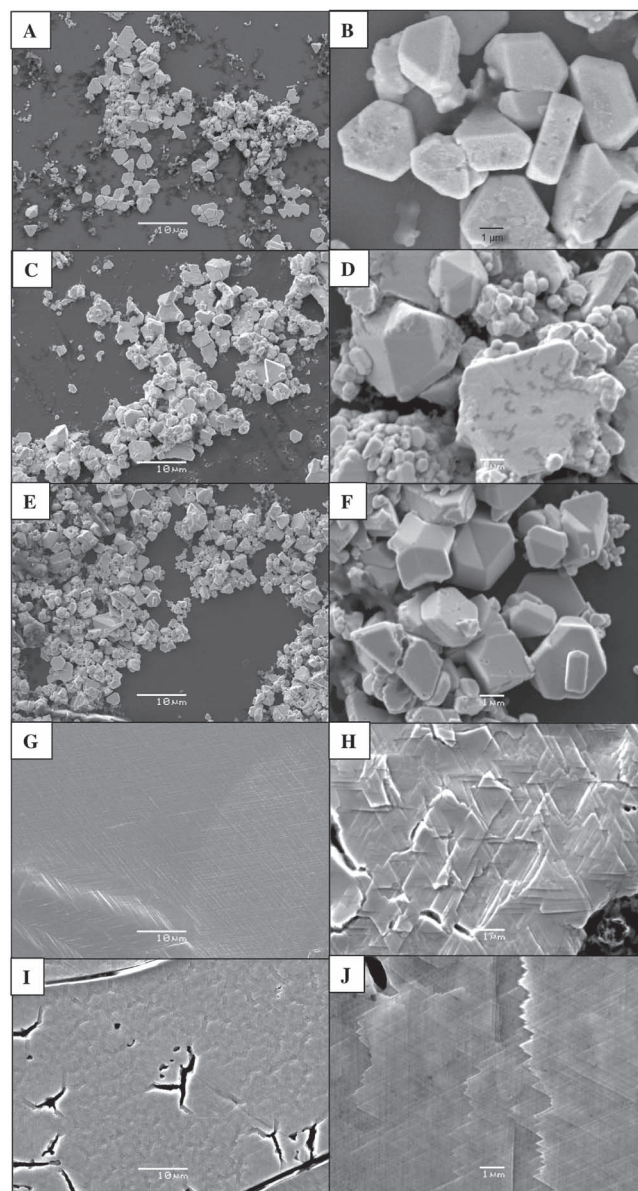


**Figure 2.** SEM picture in low and high magnification of supracrystals build with Au<sub>8</sub> (A–B), Au<sub>7</sub> (C–D), Au<sub>6</sub> (E–F), Au<sub>5</sub> (G–H) and Au<sub>4</sub> (I–J) dispersed in toluene on silicon substrate.

of at least a few tenths of a micrometer. The average interparticle distance,  $\delta$ , calculated from the  $d_{111}$  spacing (Table 1) is close to the length of the dodecanethiol all-trans configuration (1.78 nm).

Within the experimental error, no evolution of  $\delta$  with the nanocrystals diameter is present. For large nanocrystals (Au<sub>8</sub>, Au<sub>7</sub> and Au<sub>6</sub>), Figure 3A, 3C and 3E show continuous rings with discontinuous reinforcements. The reinforcements and  $d$ -spacings agree with similar fcc structures. The rings are attributed to randomly oriented supracrystals and the reinforcements in the  $[111]$  axis to well-developed supracrystals sitting on their larger flat facets. This agrees perfectly with SEM images shown in Figure 2A–F. Similar homogeneous nucleation for large Au nanocrystals has

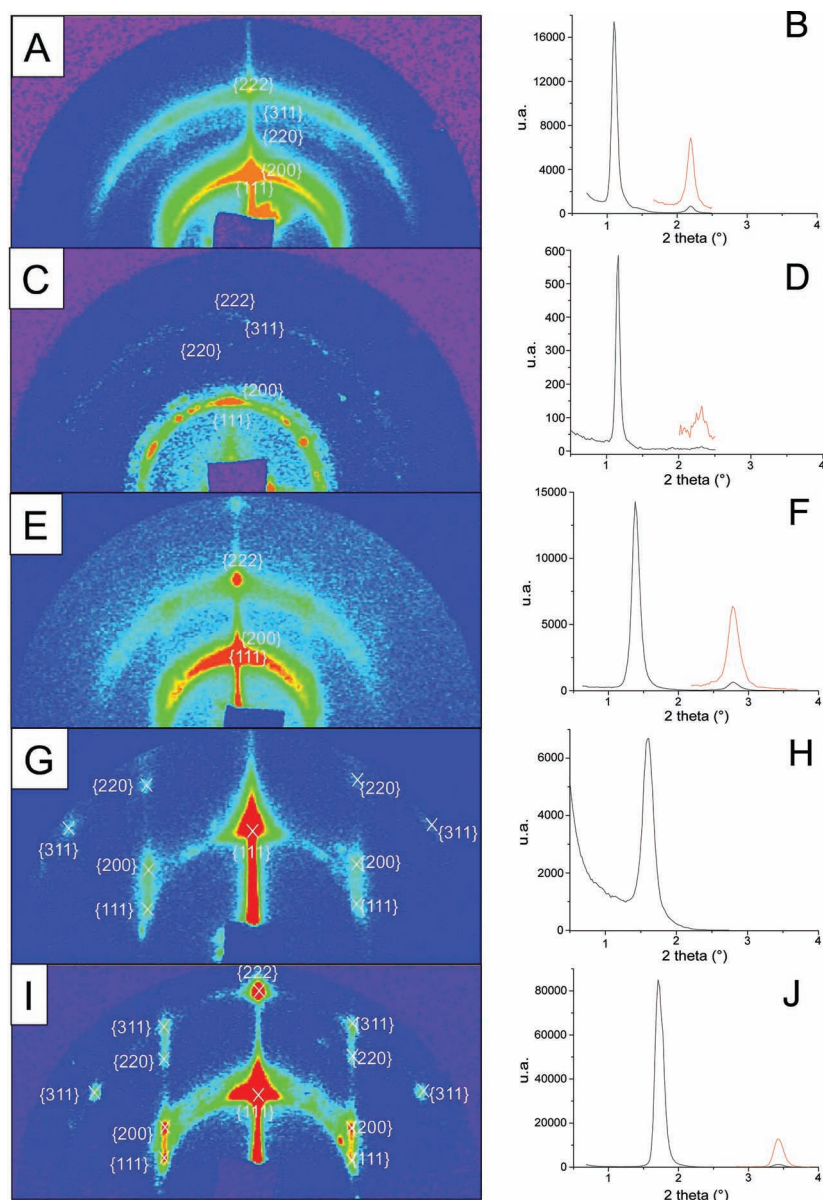


**Figure 3.** SAXRD patterns of supracrystals made of Au<sub>8</sub>, Au<sub>7</sub>, Au<sub>6</sub>, Au<sub>5</sub> and Au<sub>4</sub> (A, C, E, G, I respectively) and their corresponding profiles in the axis normal to the substrate (B, D, F, H, J).

been widely observed in various solvents.<sup>[16,18,20–22,49]</sup> The diffraction patterns for Au<sub>4</sub> and Au<sub>5</sub> (Figure 3G, I) are different from those found previously, some point reflections can be observed. The various diffraction spots are readily indexed using an fcc lattice while the [111] axis of each supracrystal is perpendicular to the substrate. This clearly indicates that the growth direction corresponds to the [111] axis. The film surface reveals lines crossing at nearly 60° or 120°. By HRSEM (Figure 4), the supracrystal surface shows some terraces with triangular structures. The corresponding linear steps have various heights, from one nanocrystal to several nanocrystals thickness. In addition to these linear steps, irregular steps with one nanocrystal thickness are observed. This agrees with a layer-by-layer growth (heterogeneous growth) for Au<sub>4</sub> and Au<sub>5</sub> nanocrystals.

These data clearly show, for the first time, that the nanocrystal size tunes the supracrystal's growth mechanism from a homogeneous to heterogeneous one. Very surprisingly, with 7-nm Co (Co<sub>7</sub>) dispersed in hexane, heterogeneous growth<sup>[7]</sup> is observed whereas, here, with a similar nanocrystal size (7 nm), homogeneous growth of Au<sub>7</sub> nanocrystals dispersed in toluene is observed. To explain such apparent discrepancies between Co<sub>7</sub> and Au<sub>7</sub> nanocrystals with similar average diameters but characterized by two various growth mechanisms, Au nanocrystals with different sizes were dispersed in hexane. Note that, the solubility of Au nanocrystals in hexane markedly drops, compared to toluene, so that there is no dispersion of Au<sub>8</sub> nanocrystals, preventing any supracrystal formation. Figure 5 shows the SEM patterns obtained for nanocrystals having an average diameter less than 8 nm. For any nanocrystal size, formation of thin films on the substrate is observed. The Figure 5 SAXD patterns insets confirm that similar fcc supracrystals are present displaying the same type of texture as found in Au<sub>4</sub> and Au<sub>5</sub> films grown in toluene (Figure 3A and 3C). No individually grown micrometric supracrystals are observed even at larger particle sizes (Au<sub>6</sub> and Au<sub>7</sub>). As with 5-nm Au nanocrystals dispersed in toluene (Figure 4), the supracrystal surface of 6-nm Au nanocrystals dispersed in hexane (Figure 6A) is made of terraces with linear steps having various heights (from one nanocrystal to several nanocrystals thickness). The mono-nanocrystals step with an irregular edge covers the entire surface. The similarity in the film morphologies, with a layer by layer growth, observed for Au<sub>4</sub> and Au<sub>5</sub> films produced by using toluene to disperse the nanocrystals (Figure 4) with those obtained with larger nanocrystals sizes (Au<sub>6</sub> and Au<sub>7</sub>) in hexane (Figure 6A) makes possible to conclude that the solvent in which the nanocrystals are dispersed is a key parameter on the crystal growth mechanism.

Even in a quasi-saturated regime, the evaporation rate of hexane remains faster (5 h) than that of toluene (7 h). To confirm that the change in the supracrystal growth mechanism is not related to the evaporation rate let us consider another solvent with a boiling point closer to toluene (b.p. = 110 °C). The Au<sub>6</sub> nanocrystals are dispersed in octane (b.p. = 125 °C) instead of hexane (b.p. = 69 °C). The evaporation time is around 8 hours as for toluene. Figure 7A and 7B clearly show formation of films with very bright SAXD reflections normal to the substrate and well-defined Bragg peaks at the resolution limit in the [111] growth axis (Figure 7A insets) indicating a layer by layer growth in fcc supracrystals, as already observed for Au<sub>6</sub> nanocrystals dispersed in hexane and also Au<sub>4</sub> and Au<sub>5</sub> nanocrystals dispersed in toluene. However, it can be seen that



**Table 1.** Summary of the Au nanocrystal properties: Average size, size distribution, center–center distance  $D$  and edge–edge distance  $\delta$ .

Sample	Diameter [nm]	Size distribution	$D$ [nm]	$\delta$ [nm]
Au <sub>4</sub>	4.3	9%	6.3	2.0
Au <sub>5</sub>	5.1	8%	6.9	1.8
Au <sub>6</sub>	5.9	8%	7.8	1.9
Au <sub>7</sub>	7.2	7%	9.3	2.1
Au <sub>8</sub>	7.8	6%	9.8	2.0

the film area is markedly reduced compared to that obtained previously. For Au<sub>6</sub> dispersed in cumene (b.p. = 152 °C) where the evaporation time is close to 48 h, the SEM images (Figure 7C and 7D) show formation of aggregates with regular shapes. The SAXD patterns and Bragg plot (Figure 7C inset) indicate a fcc crystalline structure with no preferential orientation. Note that cumene and toluene have closely related structures. Nevertheless, from these data it is concluded that the growth mechanism is controlled by the solvent nature and not by the evaporation rate. Note that the supracrystal growth mechanisms do not depend on the substrate effect. When Highly Oriented Pyrolytic Graphite replaces the silicon wafer, the crystal morphologies remain the same.

In order to understand the influence of both nanocrystal size and solvent nature on the supracrystal growth mechanism, the evaporation of Au nanocrystal solutions is simulated by Brownian dynamics and Monte Carlo methods at a particle level<sup>[49]</sup> (see above). Let us consider the interaction potential between Au nanocrystals defined by Equation (1). The potentials for the solvents toluene, hexane, octane, and cumene are compared (Figure 8). Obviously, the interactions are repulsive or very weakly attractive for hexane and octane whereas they are attractive for toluene. For cumene, the situation is less evident. Two values for the Hildebrand parameter of cumene are found in the literature: 1.75 and 1.81 MPa. This apparently minute difference in solubility parameters strongly affects the interaction potential: it is sufficient to revert from a repulsive to an attractive

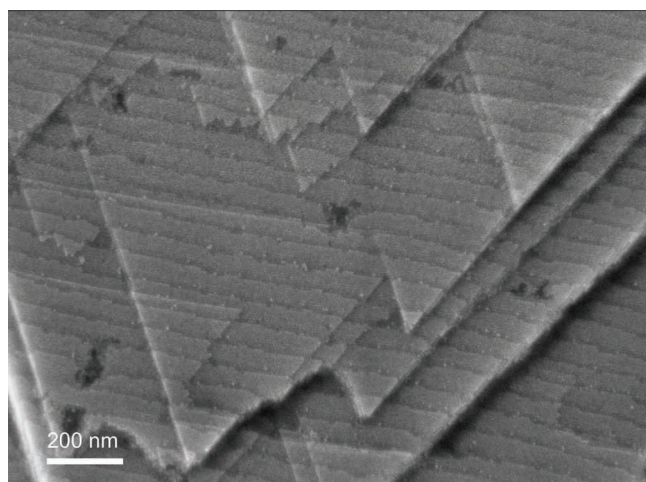


**Figure 4.** High resolution of Au<sub>5</sub> supracrystal surface deposited in toluene.

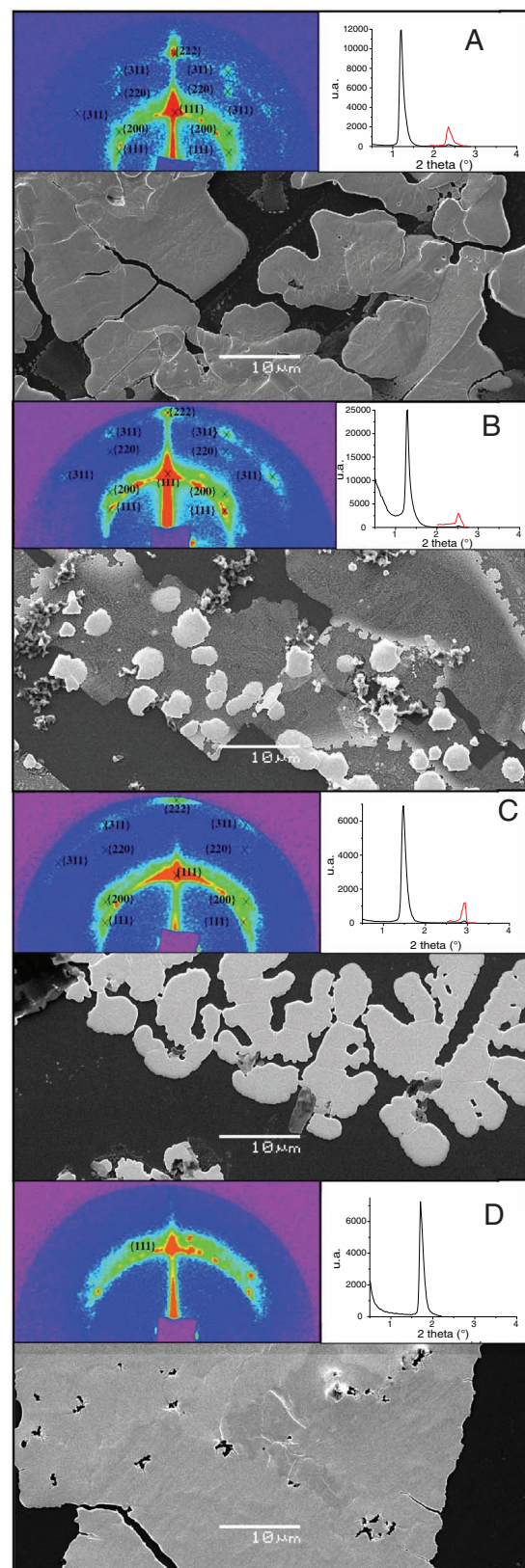


**Figure 5.** SEM picture of supracrystals built with Au<sub>7</sub> (A), Au<sub>6</sub> (B), Au<sub>5</sub> (C) and Au<sub>4</sub> (D) dispersed in hexane and deposited on silicon substrate. Inset the corresponding SAXRD characterization.

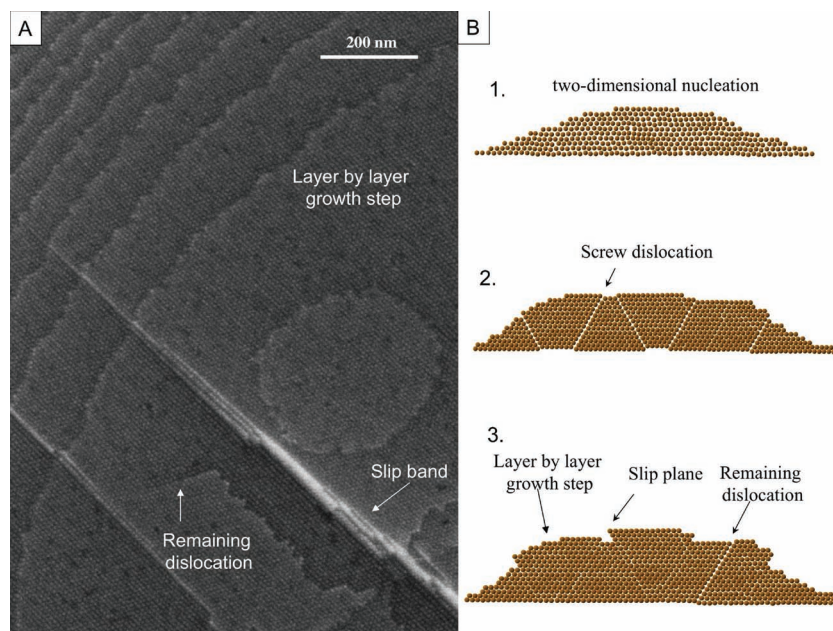


**Figure 6.** A) High resolution of Au<sub>6</sub> supracrystal surface deposited in hexane. B) Scheme illustrating the proposed mechanism of the supracrystals plastic deformation.

potential between Au<sub>6</sub> nanoparticles (Figure 8C). The interaction peak becomes more attractive with increasing nanocrystal size. This is due, on the one hand, to the dependence of the van-der-Waals term on the particle size. On the other hand, the decrease in the ligand film curvature also leads to a larger attraction between the particles. In contrast, for hexane and octane only a shallow attraction  $< kT$  is observed even at 7 nm. When the  $u_{\text{mix}}$  term in Equation (1) is neglected a more pronounced attraction peak is observed. For example for 6 nm diameter nanocrystals, the potential without the mixing term has a minimum at  $-1.19$  kT (using the new Hamaker constant), while the total energy is repulsive at the contact distance of 7.8 nm. This shows that with hexane the van der Waals attraction due to the metallic cores is compensated by the repulsion due to the ligands. As mentioned above, in Section 3, two values of the Hamaker constant can be used. Obviously, the various values of the Hamaker constant (Figure 8) have a small influence on the depth of the interaction peaks for toluene and cumene. This is attributed to the fact that the attraction is mainly due to the energy of mixing of the thiols. In particular, the change in the potential due to the variation of the nanocrystal diameter is more pronounced than the variation caused by different Hamaker constants. Note that the repulsive interactions for hexane are in agreement with recent calculations of the mean force potential for Au nanocrystals in hexane using atomistic simulations simulations.<sup>[50]</sup>

In order to understand the influence of the nanocrystal interaction on the morphology of ordered assemblies, Au nanocrystal colloidal solutions are simulated by Brownian dynamics and Monte Carlo simulations. Both approaches give the same results within the statistical accuracy of these methods. The evaporation in the experiments is so slow, that the formed structures do not depend on kinetics, but are due to the increase

in the concentration. With respect to the experimental conditions we face two major problems:

- (i) The initial nanocrystal solutions are extremely diluted (reduced density:  $5 \times 10^{-10}$ ).
- (ii) The assembly is usually observed during several hours or days.

In contrast, a usual simulation run is limited to several milliseconds (several weeks on a modern work station). Within this time in systems at the experimental dilution no particle assembly is observed since the particles do not have enough time to meet each other. Therefore, we studied nanocrystal solutions at several reduced densities ranging from  $0.5$  to  $10^{-5}$  (The particle number varies from 10000 to 100). For Au<sub>4</sub> nanoparticles in toluene, no cluster formation is observed even at the highest densities (Figure 9A). For Au<sub>5</sub> nanoparticles, clusters nucleate starting from a density of 0.004 (volume fraction: 0.002) (Figure 9B). This is in good agreement with the simulations by Kahn et al.<sup>[36]</sup> where cluster formation for volume fractions larger than

0.0027 is observed. In diluted systems for Au<sub>6</sub> and Au<sub>7</sub> nanoparticles, the first small clusters appear which may grow due to cluster-cluster aggregation (Figure 9C and 9D). Usually all clusters have compact hexagonal structures with a random order of layers. We have carried out simulations at the same densities using the interaction potential predicted above for hexane. No cluster formation even for large particles or high densities is observed (Figure 9I, 9J, 9K and 9L). Obviously, an attraction peak of at least  $-3$  kT is necessary to observe the homogeneous nucleation of Au nanocrystals. To study the influence of evaporation on the morphology and superlattice ordering, the evaporation process is modeled as follows: a wall at the bottom of the simulation box represents the substrate. The wall-particle interaction is defined by a steric repulsion due to the coating molecules and a van der Waals interaction between a sphere and a half-space.<sup>[49]</sup> At the top of the box, there is a liquid-gas interface, which slowly moves down during evaporation. This interface is made of the solvent and the coating of the particles crossing the interface. When a particle crosses the liquid-gas interface, the area of this interface increases due to the curvature of the particle. This leads to an increase in the surface energy that confines the particles within the solution layer. The interaction model previously described<sup>[49]</sup> is used. The evaporation speed used in the simulations is much faster than the experimental value, which is determined by the boiling point of the solvent. A systematic variation of the evaporation speed in the simulations has shown that the speed used here is sufficiently large to predict qualitatively the morphology of structures. However, the size of the organizations increases at slower evaporation, which may explain the difference in size between the superlattice crystals obtained by experiments and simulations.

Evaporation of a colloidal solution is simulated varying the nanoparticle diameter from 4 to 7 nm. Simulations are started



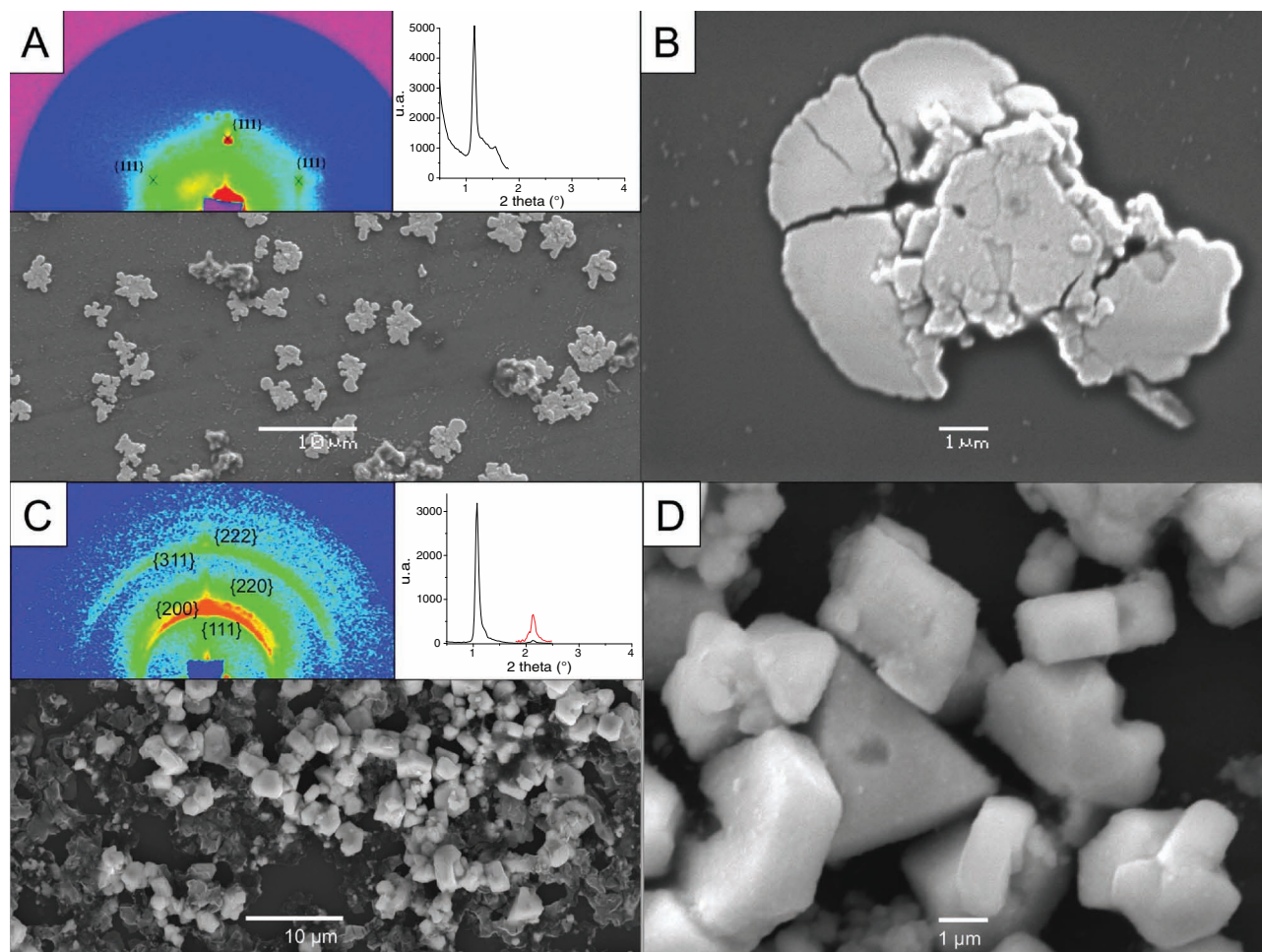


**Figure 7.** SEM picture of supracrystals build with  $\text{Au}_6$  dispersed in A–B) octane and C–D) cumene and their corresponding SAXRD characterization inset.

from a diluted solution (reduced density:  $3 \times 10^{-3}$ ), which leads after evaporation to the formation of 3D superlattice crystals. We first study the case of toluene as solvent. For  $\text{Au}_4$ , a film of an assembly of well-ordered 3D nanoparticles is observed at the end of the evaporation (Figure 9E). For  $\text{Au}_5$ , a coexistence of spherical clusters and free particles occurs (Figure 9F). For  $\text{Au}_6$  and larger nanoparticles, small superlattices of globular shape form when the simulation starts. During the evaporation the superlattices coalesce to form larger assemblies (Figure 9G and 9H). In contrast with hexane, layers of well-ordered assemblies are observed at any nanocrystal sizes (Figure 9M, 9N and 9P). Good agreement between the structures observed in experiments (Figure 2) and simulations (Figure 9) is obtained. For 6 and 7 nm nanocrystals in toluene (Figure 2A–F), large clusters, made of ordered nanocrystals, are produced as well described by simulations (Figure 9G, 9H) explained by homogeneous nucleation. Conversely with 4 nm nanocrystals, a layer-by-layer growth process is observed experimentally (Figure 2I,J) and from simulation (Figure 9E). For 5 nm nanocrystals, simulations show that the formation of clusters depends on the nanocrystals concentration (Figure 10). This may explain why individual supracrystals are not observed in experiments

(Figure 2G, 2H). In agreement with the experiment, ordered layers are observed for hexane at any nanocrystals size, while it occurs in toluene only with small particles ( $\text{Au}_4$ ). The order is attributed to the compression of nanoparticles by the solution-air interface at the end of the evaporation. For larger nanocrystals in toluene, superlattices already form within the solution due to a nucleation process mainly caused by solvent inter-mediated ligand attraction.

Note that the degree of cluster formation does not markedly change with the two Hamaker constant values. As an example we show the cluster formation for  $\text{Au}_5$  nanoparticles in toluene as a function of the density (Figure 10). Comparison of both curves indicates that the change in the Hamaker constant has only a very slight influence on the threshold concentration for the nucleation of nanocrystal assemblies. It should be noted that the larger particles form interconnected structures at higher densities due to the strong attraction between the particles.

With octane as solvent, a film of an assembly of well-ordered 3D nanoparticles is observed at the end of the evaporation in good agreement with the experiment (Figure 11D). In contrast, for cumene, the results depend on the used Hildebrand parameter. For 1.75 MPa an organized film is obtained



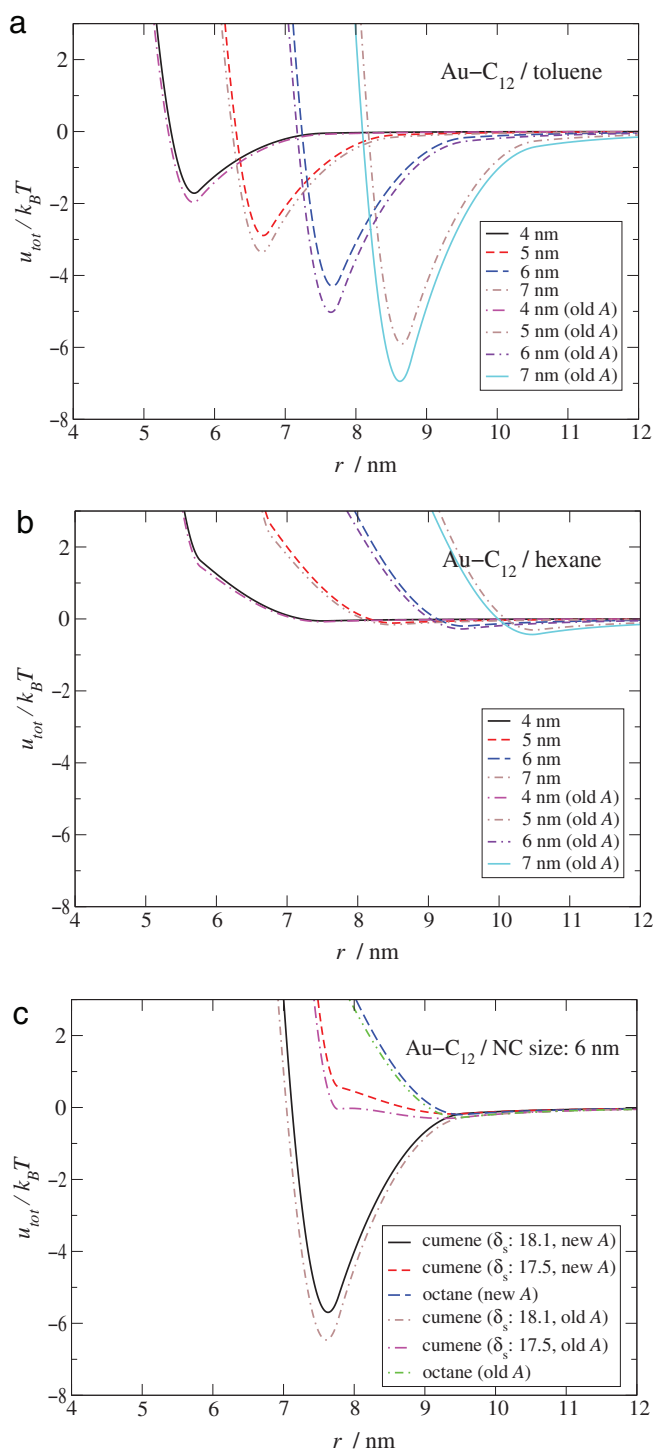


**Figure 8.** Interaction potentials between two gold nanocrystals coated by dodecanethiol in different solvents: A) toluene, B) hexane, C) cumene and octane. All potentials are calculated at 25 °C.

(Figure 11D), while for 1.81 MPa individual clusters appear at the end of evaporation (Figure 11F). Experimentally, individual supracrystals are observed (Figure 7C–D) indicating that the larger value for the Hildebrand parameter of cumene is probably correct.

Hence, either an experimental point of view or simulations lead to the conclusion that a transition from a layer-by-layer growth (heterogeneous) to homogeneous nucleation in toluene between 5 nm to 6 nm occurs. The facets of the supracrystals are related to a transition to a solid phase expected for very short-range attraction potentials, as in our case. Without the attraction due to the coating, the transition to supracrystals is observed in simulations at a NC diameter of 9 nm. In hexane and octane our theoretical model predicts repulsion between the ligands, which explains the absence of homogenous nucleation observed in experiments.

In the following a tentative mechanism of heterogeneous and homogeneous supracrystal growths is proposed. Here with the same capping agent and same nanocrystal size, the solvent tunes the growth mechanism of supracrystals. We know from previous simulations<sup>[50]</sup> that, in vacuum, the van der Waals interaction between Au cores is weak compared to the total interaction including the attraction between the capping molecules. However, the situation is somewhat more difficult when the solvent is taken into account. In this case the total interaction between the nanocrystals is given by the interplay of solvent–solvent, solvent–surfactant, surfactant–surfactant interactions. This leads to the well-known good solvent effect due to the strong attractive interaction between solvent and surfactant compensating solvent–solvent and surfactant–surfactant interactions. Consequently, the total interaction turns from attractive to repulsive.<sup>[51]</sup> In the case of toluene the situation is reversed with a strong solvent–solvent attraction. Therefore, with toluene as solvent we could expect, when the van der Waals interactions due to the core of nanocrystals are strong enough (i.e.,  $D > 5$  nm), the total attractive interactions between two particles will lead to supracrystal growth in solution (homogeneous growth). Hexane, considered as a good solvent, will favor layer-by-layer growth. The solvent effect will be the major parameter in the control of the supracrystal growth. Hence, for homogeneous nucleation in solution, because of the strong attractive interactions between the nanocrystals, the particles come into contact with highly efficient alkyl chain interdigitation expelling the solvent from the chains. Then, the cohesive forces due to the strong intrinsic attractive interactions between the carbon atoms of the chains<sup>[50]</sup> could favor formation of a rather stiff material. The control of the shape of the final materials is then governed by the arrangement of the maximum density of hard spheres packed in face centered cubic (fcc) superlattices with the formation of tetrahedral subunits corresponding to the densest possible packing of four spheres, as described by Kepler<sup>[52]</sup> in 1611. For heterogeneous growth corresponding to a layer-by-layer process, during the evaporation process the growth by two-dimensional nucleation leads to a single nanocrystals step. At the final stage of the evaporation process (Figure 6B-1) a “soft solid” is produced by layer stacking of nanocrystals having some solvent molecules remaining in their surroundings. A further dry process leads to dislocations (Figure 6B-2). At the final stage, the crystal tends to relax to a more stable state, some crystals block slip along their slip planes by dislocation displacement (Figure 6B-3). This movement, called plastic deformation<sup>[53]</sup> needs a mechanical stress that may be built up by the various evaporation rates at the various places in the crystal. The slip plane corresponds to the plane where the nanocrystals are most closely packed, here in fcc this is the {111} plane. The proposed mechanism demonstrates that

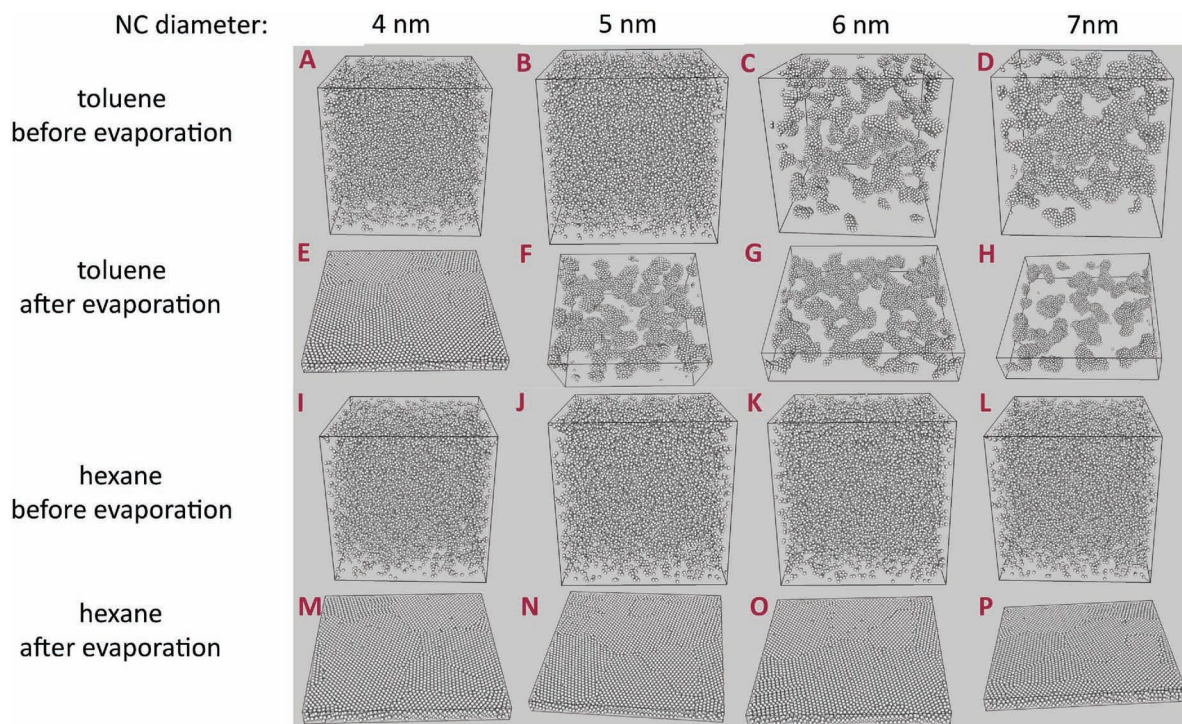


**Figure 9.** Snapshots of a system of gold nanocrystals obtained by Brownian dynamic simulations under the conditions indicated in the figure.

the supracrystals exhibit a certain amount of ductility when the nanocrystals are in weak attractive or repulsive conditions. In contrast, the supracrystals made of the largest nanocrystals do not show any dislocation (Figure S1, Supplementary Information). We could expect more brittle properties for these crystals than the film. If the supracrystal has few or any dislocations, it cannot relax its mechanical stress through plastic deformation and break up. This cannot be related to the growth mechanism proposed by Korgel et al.<sup>[20]</sup> for Au nanocrystals in chloroform, from which a growth on dislocation is claimed. One of the differences

is the lack of a spiral growth feature and dislocation on the top monolayer<sup>[54]</sup> (Figure 6A).

## 5. Conclusions

In conclusion, it is shown from experiments that the degree of affinity of the solvent for the coating agent is as important a parameter as the nanocrystal size to the determination of the final morphology of supracrystals grown by evaporation of Au nanocrystal solutions. In order to be predictive, simulations necessarily include a free mixing energy term, as presently done. Good agreement with experimental observations cannot be reached by considering the van der Waals attraction alone. Subtle changes in the Hildebrand solubility parameter strongly impact the interaction potential and are sufficient to switch from an attractive to a repulsive situation, i.e., from a homogeneous to a heterogeneous growth.

## 6. Experimental Section

All products and solvents were purchased from a variety of sources and used without purification. Toluene (>98%) was procured from Riedel de Haën, and ethanol (99.8%) from Prolabo. Chlorotriphenylphosphine gold(I) (98%) and tert-butylamine borane complex (>97%) were from STREM. 1-dodecanethiol and boran-ammonia complex (97%) were from Aldrich. The water used was purified with a Milipore system (18.2 M $\Omega$ ). Transmission Electron Microscopy (TEM), High Resolution Electron Microscopy (HRTEM) and Scanning Electron Microscopy (SEM) images were obtained with a JEOL JEM 1011 or JEOL JEM 2010 and JEOL JSM-5510LV instruments, respectively. Small Angle X-Ray Diffraction (SAXD) measurements were made with a home-made, copper anode system.

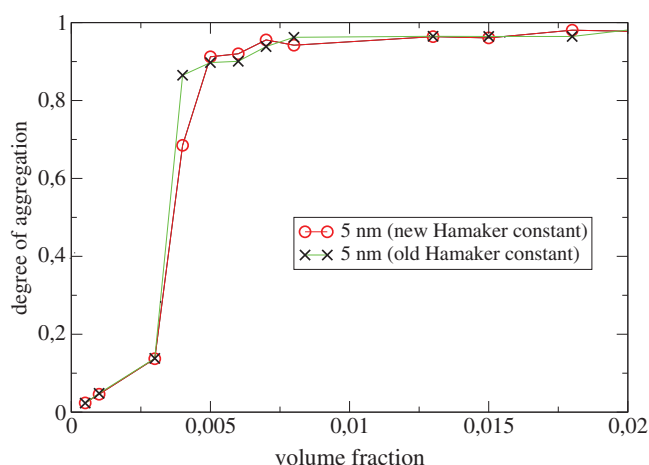


**Figure 10.** Degree of aggregation of gold nanocrystals obtained by Brownian dynamic simulations at different temperatures. The nanocrystals are coated by dodecanethiol and dispersed in toluene.



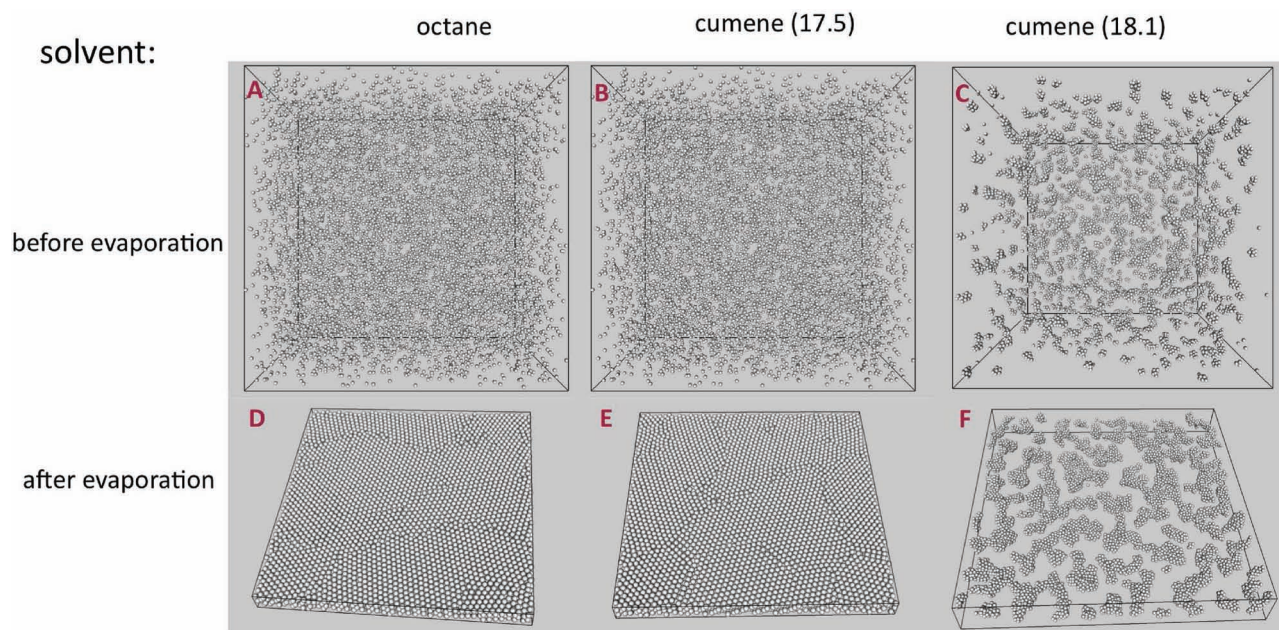


**Figure 11.** Snapshots of a system of gold nanocrystals obtained by Brownian dynamic simulations under the conditions indicated in the figure.

## Supporting Information

Supporting Information is available from the Wiley Online Library or from the author.

## Acknowledgements

The research leading to these results has received funding from the European Community's Seventh Framework Programme (FP7/2008–2011) under Grant Agreement n° 213382. The M.P.P. research leading to these results has received funding from an advanced Grant of European Research Council under grant agreement 267/29.

Received: February 18, 2011  
Published online: June 3, 2011

- [1] H. Kroto, *Science* **1988**, 242, 1139–1145.
- [2] D. A. Bazylinski, R. B. Frankel, *Nat. Rev. Micro.* **2004**, 2, 217–230.
- [3] M. S. Del Rio, P. Martinetto, C. Reyes-Valerio, E. Dooryhee, M. Suarez, *Archaeometry* **2006**, 48, 115–130.
- [4] M. Reibold, N. Pätzke, A. A. Levin, W. Kochmann, I. P. Shakhverdova, P. Paufler, D. C. Meyer, *Crystal. Res. Technol.* **2009**, 44, 1139–1146.
- [5] J. V. Sanders, *Nature* **1964**, 204, 1151–1153.
- [6] E. Alphantery, Y. Ding, A. T. Ngo, Z. L. Wang, L. F. Wu, M. P. Pileni, *ACS Nano* **2009**, 3, 1539–1547.
- [7] M. P. Pileni, *J. Phys. Chem. B* **2001**, 105, 3358–3371.
- [8] M. P. Pileni, *Acc. Chem. Res.* **2008**, 41, 1799–1809.
- [9] M. P. Pileni, *Acc. Chem. Res.* **2007**, 40, 685–693.
- [10] H. Fudouzi, Y. Xia, *Langmuir* **2003**, 19, 9653–9660.
- [11] C. R. Kagan, C. B. Murray, M. G. Bawendi, *Phys. Review B* **1996**, 54, 8633.
- [12] A. Courty, A. Mermet, P. A. Albouy, E. Duval, M. P. Pileni, *Nat. Mater.* **2005**, 4, 395–398.
- [13] D. V. Talapin, E. V. Shevchenko, C. B. Murray, A. V. Titov, P. Kral, *Nano Lett.* **2007**, 7, 1213–1219.
- [14] A. R. Tao, D. P. Ceperley, P. Sinsermsuksakul, A. R. Neureuther, P. Yang, *Nano Lett.* **2008**, 8, 4033–4038.
- [15] Z. Nie, A. Petukhova, E. Kumacheva, *Nat. Nano* **5**, 15–25.
- [16] B. L. V. Prasad, C. M. Sorensen, K. J. Klabunde, *Chem. Soc. Rev.* **2008**, 37, 1871–1883.
- [17] K. J. M. Bishop, C. E. Wilmer, S. Soh, B. A. Grzybowski, *Small* **2009**, 5, 1600–1630.
- [18] S. I. Stoeva, B. L. V. Prasad, S. Uma, P. K. Stoimenov, V. Zaikovski, C. M. Sorensen, K. J. Klabunde, *J. Phys. Chem. B* **2003**, 107, 7441–7448.
- [19] R. L. Whetten, M. N. Shafigullin, J. T. Khoury, T. G. Schaaff, I. Vezmar, M. M. Alvarez, A. Wilkinson, *Acc. Chem. Res.* **1999**, 32, 397–406.
- [20] M. B. Sigman, A. E. Saunders, B. A. Korgel, *Langmuir* **2003**, 20, 978–983.
- [21] B. Abecassis, F. Testard, O. Spalla, *Phys. Rev. Lett.* **2008**, 100, 115504.
- [22] H. Yan, S. Cingarapu, K. J. Klabunde, A. Chakrabarti, C. M. Sorensen, *Phys. Rev. Lett.* **2009**, 102, 095501.
- [23] O. C. Compton, F. E. Osterloh, *J. Am. Chem. Soc.* **2007**, 129, 7793–7798.
- [24] S. Y. Park, A. K. R. Lytton-Jean, B. Lee, S. Weigand, G. C. Schatz, C. A. Mirkin, *Nature* **2008**, 451, 553–556.
- [25] M. O. Robbins, K. Kremer, G. S. Grest, *J. Chem. Phys.* **1988**, 88, 3286–3312.
- [26] P. G. Bolhuis, D. Frenkel, S.-C. Mau, D. A. Huse, *Nature* **1997**, 388, 235–236.
- [27] A. Taylor, B. Kagle, *Crystallographic Data on Metal and Alloy Structures*, Dover Publications, New York **1963**.
- [28] J. E. Hearn, R. L. Johnston, S. Leoni, J. N. Murrell, *J. Chem. Soc., Faraday Trans.* **1996**, 92, 425–432.
- [29] O. Kitakami, H. Sato, Y. Shimada, F. Sato, M. Tanaka, *Phys. Rev. B* **1997**, 56, 13849.
- [30] S. H. Tolbert, A. P. Alivisatos, *Z. Phys. D: At. Mol. Clusters* **1993**, 26, 56–58.
- [31] S. H. Tolbert, A. P. Alivisatos, *J. Chem. Phys.* **1995**, 102, 4642–4656.

- [32] A. I. Henry, A. Courty, M. P. Pileni, P. A. Albouy, J. Israelachvili, *Nano Lett.* **2008**, *8*, 2000–2005.
- [33] N. Goubet, J. Richardi, P. A. Albouy, M. P. Pileni, *J. Phys. Chem. Lett.* **2011**, 417–422.
- [34] E. Verwey, J. Overbeek, *Theory of the Stability of Lyophobic Colloids*, Dover Publications, **1999**.
- [35] P. C. Ohara, D. V. Leff, J. R. Heath, W. M. Gelbart, *Phys. Rev. Letters* **1995**, *75*, 3466.
- [36] S. J. Khan, F. Pierce, C. M. Sorensen, A. Chakrabarti, *Langmuir* **2009**, *25*, 13861–13868.
- [37] D. Bargeman, F. van Voorst Vader, *J. Electroanal. Chem.* **1972**, *37*, 45–52.
- [38] M. D. Croucher, M. L. Hair, *J. Phys. Chem.* **1977**, *81*, 1631–1636.
- [39] L. Motte, F. Billoudet, M. P. Pileni, *J. Phys. Chem.* **1995**, *99*, 16425–16429.
- [40] R. Evans, J. B. Smitham, D. H. Napper, *Colloid Polym. Sci.* **1977**, *255*, 161–167.
- [41] J. B. Smitham, R. Evans, D. H. Napper, *J. Chem. Soc., Faraday Trans. 1* **1975**, *71*, 285–297.
- [42] G. E. Poirier, E. D. Pylant, *Science* **1996**, *272*, 1145–1148.
- [43] A. F. M. Barton, *Chem. Rev.* **1975**, *75*, 731–753.
- [44] A. F. M. Barton, *Handbook of Solubility Parameters and other Cohesion Parameters*, CRC Press, Boca Raton **1983**.
- [45] M. P. Allen, *Mol. Phys.* **1980**, *40*, 1073–1087.
- [46] M. Allen, D. Tildesley, *Computer Simulation of Liquids*, Clarendon Press, New York **1993**.
- [47] N. Zheng, J. Fan, G. D. Stucky, *J. Am. Chem. Soc.* **2006**, *128*, 6550–6551.
- [48] S. M. Rupich, E. V. Shevchenko, M. I. Bodnarchuk, B. Lee, D. V. Talapin, *J. Am. Chem. Soc.* **2009**, *132*, 289–296.
- [49] Y. Lalatonne, J. Richardi, M. P. Pileni, *Nat. Mater.* **2004**, *3*, 121–125.
- [50] P. Schapotschnikow, R. Pool, T. J. H. Vlugt, *Nano Lett.* **2008**, *8*, 2930–2934.
- [51] N. Patel, S. A. Egorov, *J. Chem. Phys.* **2007**, *126*, 054706–054707.
- [52] J. Kepler, *Strena Seu de Nive Sexangula*; Caspar, M., Hammer, F., Eds.; Clarendon Press: Oxford, **1966**; p 46.
- [53] A. Cottrell, *Dislocations and Plastic Flow in Crystals*, Clarendon Press, Oxford, **1965**.
- [54] W. Read, *Dislocations in Crystals*, McGraw-Hill, New York **1953**.